



## Early Identification of Reservoir-Bank Landslides in Deeply Incised Mountain Canyon Areas with Interferometric Baseline Optimization

Wenfei XI<sup>1,2,3</sup>, Wenyu HONG<sup>1</sup>, Zhiqian YANG<sup>4</sup>, Guangcai HUANG<sup>5,6</sup>, Junqi GUO<sup>1</sup>, Kunwu YANG<sup>1</sup>, Tingting JIN<sup>1</sup>

<sup>1</sup>Faculty of Geography, Yunnan Normal University, Kunming Yunnan 650500, China;

<sup>2</sup>Key Laboratory of Highland Geographic Processes and Environmental Change in Yunnan Province, Kunming, Yunnan 650500, China;

<sup>3</sup>Key Laboratory of Early Rapid Identification, Prevention and Control of Geological Diseases in Traffic Corridor of High Intensity Earthquake Mountainous Area of Yunnan Province, Kunming, Yunnan 650093, China;

<sup>4</sup>School of Public Safety and Emergency Management, Kunming University of Science and Technology, Kunming, Yunnan 650093, China;

<sup>5</sup>Guizhou Geological Survey, Guiyang, Guizhou 550081, China;

<sup>6</sup>Engineering Tecmology Innovation Center of Mineral ResourcesExploraions in Bedroek Zones, Ministry of Naur Resources, Guiyang 550081;

*Correspondence to:* Wenfei XI([wenfeixi@ynnu.edu.cn](mailto:wenfeixi@ynnu.edu.cn))

**Abstract:** The complex geological conditions in deeply incised mountainous canyon areas make reservoir-bank landslides a frequent hazard. Accurate interferogram selection and baseline network configuration are crucial for SBAS-InSAR-based landslide monitoring, yet are severely challenged by seasonal vegetation decorrelation. To overcome this limitation, this study proposes a novel vegetation-adaptive weighted coherence threshold method that integrates time-series vegetation dynamics into interferometric baseline optimization. This approach establishes a vegetation-coherence coupling model to dynamically adjust coherence thresholds based on quantified vegetation coverage levels and synergizes ERA5 meteorological data with tropospheric delay modeling for atmospheric correction. The results demonstrate significant advancements: (1) The deformation rate standard deviation is reduced by 0.520 and 0.192 compared to traditional short-temporal baseline and average coherence threshold methods, respectively, corresponding to a 29.1% improvement (1.2668 vs. 1.7865). (2) 140,146 additional valid phase-unwrapping points were obtained, indicating substantially improved interferometric processing quality. (3) 39 landslides were successfully identified, representing a 22% increase compared to conventional methods (32 landslides), with 7 new high-risk sites discovered even during low-coherence vegetation seasons. Based on field verification with drone surveys, typical landslides were selected to analyze their spatial distribution and temporal evolution patterns, demonstrating the applicability of the method in deeply incised mountainous canyon areas. These findings provide



theoretical and technical support for regional disaster prevention and mitigation efforts.

**Keywords:** SBAS-InSAR; WCTM Method Interferometric baseline; Reservoir Bank Landslide; Early Identification

## 1 Introduction

2 Landslides along reservoir banks are a common geological hazard during the construction and operation of hydraulic  
3 and hydropower engineering projects(Liu et al., 2022; Li et al., 2021). These landslides are typically concentrated on  
4 the steep slopes on both sides of deeply incised mountain canyon reservoir banks(Zhu et al., 2024; Lu et al., 2019).  
5 Early identification of reservoir-bank landslides is a crucial component of geological hazard prevention and risk  
6 assessment. Traditional technologies, such as Global Navigation Satellite Systems (GNSS) (Guo et al.,2025; Mao et  
7 al.,2024)and optical remote sensing(Cai et al.,2024; Guo et al., 2016), are unable to meet the current demands for  
8 landslide detection. In contrast, Synthetic Aperture Radar Interferometry (InSAR) has shown significant potential(Li  
9 et al., 2020; Li et al., 2022; Zhou et al., 2022). Deformation monitoring technology based on InSAR baseline  
10 optimization has become a key method for high-precision early landslide identification(Ferretti et al., 2001; Pepe, 2021;  
11 Liao et al., 2021). However, SBAS-InSAR technology requires high-quality interferograms and a well-constructed  
12 baseline network. Incorrect or inaccurate selection of interferograms and baseline network configurations may  
13 introduce decorrelation errors and systematic errors, reducing the accuracy of deformation inversion or even preventing  
14 correct inversion of deformation results(Zebker et al., 2021; Zhang et al., 2022). Additionally the accuracy of landslide  
15 monitoring is influenced by multiple factors, such as decorrelation caused by complex terrain, coherence fluctuations  
16 due to land cover changes, and the rational configuration of interferometric baseline optimization parameters( Liu et  
17 al., 2024; Ren et al., 2022; Wang et al., 2023; Zhang et al., 2022). Selecting high-quality interferograms and optimizing  
18 the interferometric baseline network in the extreme natural conditions of deeply incised mountain canyon regions has  
19 become an important research topic for large-scale reservoir bank landslide identification and monitoring.  
20 Currently, the methods for interferogram selection and baseline optimization can generally be divided into three  
21 categories: The first category is expert knowledge-based manual selection of interferograms. In this approach, expert  
22 knowledge is used to conduct empirical analysis of all acquired interferograms. The interferograms with higher  
23 coherence are selected through manual judgment based on coherence comparisons. For example, Shi et al., (2019)  
24 manually selected interferograms with higher coherence based on empirical knowledge to study the surface response  
25 and underground characteristics during the groundwater extraction restriction period in Suzhou. Although this method



26 can effectively reduce the impact of spatiotemporal decorrelation in forested areas with extremely low coherence, it is  
27 highly subjective due to reliance on expert knowledge, and is time-consuming and labor-intensive. Additionally, it  
28 fails to meet the deformation monitoring requirements for long-term time-series landslide detection in large-scale  
29 reservoir banks.

30 The second category of methods involves selecting interferograms by simultaneously setting temporal baseline and  
31 spatial baseline thresholds. During the SBAS-InSAR processing, interferograms are selected based on short time  
32 baseline and spatial baseline thresholds, which are determined through pre-experimental comparative analysis or prior  
33 knowledge. For example, [Zhao et al., \(2012\)](#) used ALOS PALSAR2 data for large-scale landslide detection in Southern  
34 California and Oregon, while [Zhou et al., \(2023\)](#) utilized Sentinel-1 data to monitor permafrost changes in the XiaoTuo  
35 River region, both of which set short time and space baseline thresholds for interferogram selection. Although setting  
36 short time and spatial baseline thresholds is the most widely used method for interferogram selection, this approach is  
37 based on the empirical assumption that ground objects undergo minimal changes over short time intervals, which will  
38 not induce spatiotemporal decorrelation. However, this assumption does not guarantee that all interferogram pairs will  
39 exhibit good coherence. On the contrary, setting excessively short time and spatial baseline thresholds can introduce  
40 decorrelation and systematic errors, reducing the accuracy of deformation inversion results.

41 The third category of methods is based on coherence coefficient for interferogram selection, where interferograms are  
42 chosen by setting a coherence coefficient threshold and optimizing the interferometric baseline network. For example,  
43 [Tao et al.,\(2021\)](#)used a custom coherence coefficient threshold for interferogram selection; [Wang et al.,\(2022\)](#); [Wang](#)  
44 [et al.,\(2023\)](#)et al. directly used the average coherence between SAR images as a baseline constraint indicator to  
45 optimize interferogram selection; [Zhang et al.,\(2024\)](#)used average segmented coherence threshold coefficients to select  
46 interferograms in landslide creep identification and monitoring in the Xiaojiang River Basin. The coherence coefficient  
47 of InSAR interferograms is influenced by the spatiotemporal baseline of SAR images and external environmental  
48 coupling, which can accurately reflect the quality of the interferogram. Setting a coherence coefficient threshold is a  
49 reliable method for generating a robust interferometric baseline network. Custom coherence coefficient thresholds are  
50 often established through prior knowledge or comparative pre-experiments. However, this method is highly subjective  
51 and suffers from issues such as insufficient interferogram samples for pre-experiments. Moreover, the set thresholds  
52 cannot account for the intermittent coherence problems caused by vegetation changes, while the average coherence  
53 coefficient threshold overly relies on simple statistical patterns and fails to consider the impact of vegetation cover  
54 changes on the coherence of interferograms.



55 In summary, compared to other interferometric baseline optimization methods, expert knowledge-based manual  
56 selection of interferograms is the most time-consuming and labor-intensive approach, making it unsuitable for long-  
57 term landslide deformation monitoring along reservoir banks. Although methods based on simultaneous setting of  
58 temporal/spatial baseline thresholds and those using coherence coefficient for interferogram selection have improved  
59 upon traditional expert-based approaches, these methods remain highly subjective and fail to cover all potential  
60 baseline selection errors. They may also introduce decorrelation and systematic errors, thereby affecting the accuracy  
61 of deformation inversion and limiting their applicability in complex environments. Furthermore, they inadequately  
62 account for the impacts of external environmental conditions on coherence(Dai et al., 2022; Westerhoff et al., 2020;  
63 Zhang et al., 2023). For instance, the application of InSAR in low-coherence areas such as mountainous canyon regions  
64 and vegetated zones faces considerable limitations(Lemmetynen et al., 2022) The combination of temporal and spatial  
65 baselines is critical in deformation monitoring; ideally, baseline combinations should maintain high coherence while  
66 ensuring the precision of deformation signal extraction. However, certain temporal and spatial baseline combinations  
67 may exhibit superficially high coherence but result in distortion of deformation information due to terrain shielding,  
68 vegetation changes, or other interfering factors, ultimately failing to produce ideal interferograms(Chen et al., 2021;  
69 Santoro et al., 2009).

70 This issue of neglecting the impact of vegetation coverage changes on coherence can be addressed by considering the  
71 variation in vegetation coverage over time and introducing a weighted average coherence coefficient to optimize the  
72 interferometric baseline network. For example, during InSAR processing, it is observed that vegetation coverage is  
73 relatively sparse in winter, leading to good coherence between SAR images even over longer temporal intervals.  
74 Conversely, in summer, when vegetation coverage is dense, coherence between SAR images may be poor even over  
75 shorter temporal intervals. We propose that such anomalous baseline combinations represent potential issues in  
76 interferometric baseline optimization. First, vegetation coverage is calculated over time. Then, interferograms are  
77 categorized into grades, and using the weighted average coherence of the categorized interferograms  
78 as the coherence coefficient threshold, it is possible to optimize the interferometric baseline network. Additionally  
79 analyzing the low-frequency anomalous patterns in baseline combinations can effectively mitigate decorrelation issues  
80 in interferograms, thereby providing a more reliable baseline optimization strategy for the early identification of  
81 landslides along deeply incised mountainous reservoir banks.

82 The main objective of this study is to address the coherence issues caused by the impact of vegetation on interferogram  
83 acquisition, which has been overlooked in previous SBAS-InSAR baseline network optimization methods. A weighted



84 coherence threshold method (WCTM) that considers vegetation coverage changes is proposed to optimize the  
85 interferometric baseline network. First, the vegetation coverage in the study area is calculated, and interferograms are  
86 categorized based on predefined vegetation coverage grades. Then, the weighted average coherence of the categorized  
87 interferograms is calculated and used as the coherence coefficient threshold to optimize the baseline network.  
88 Additionally the fifth-generation atmospheric reanalysis product (ERA-5) is introduced to mitigate atmospheric delay  
89 errors. Finally, SBAS-InSAR processing is performed using the optimized interferometric baseline and corrected  
90 atmospheric delay errors to identify and monitor large-scale reservoir-bank landslides, analyzing their spatiotemporal  
91 distribution characteristics and evolutionary patterns.

## 92 **2. Study Area and Research Data**

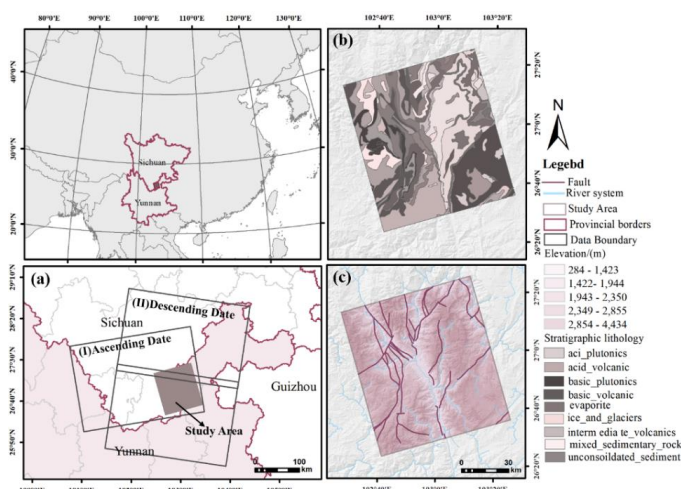
### 93 **2.1 Study Area**

94 The Baihetan Reservoir is located in the lower reaches of the Jinsha River, at the confluence of Sichuan and Yunnan  
95 provinces, and is one of China's key hydropower projects (Fig.1a). The reservoir area is situated at the northeastern  
96 edge of the Hengduan Mountains and the southeastern margin of the Tibetan Plateau. characterized by complex  
97 geographical and geological features. The reservoir covers approximately 7,285.72 km<sup>2</sup> with a linear distribution. The  
98 terrain is primarily dominated by deeply incised river valleys and high mountain gorges, with diverse  
99 geomorphological types(Li et al., 2022), including river erosion, tectonic, and glacial erosion landforms(Xi et al.,2020).  
100 The region exhibits significant elevation variation, ranging from a minimum elevation of 284 m to a maximum of  
101 4,434 meters, with a relative elevation difference of up to 3,950 meters. (Shi et al.,2022; Zhu et al.,2021), typical of a  
102 deeply incised alpine gorge region(Xie et al., 2012).

103 The climate of the area is classified as a subtropical plateau monsoon climate, characterized by distinct wet and dry  
104 seasons, with an average annual precipitation of 822.7 mm. Precipitation is predominantly concentrated in the wet  
105 season, while the dry season is relatively arid. Due to the unique climatic conditions and abundant water resources, the  
106 stratigraphy of the reservoir area is complex, spanning multiple geological periods, including the Quaternary, Permian,  
107 and Carboniferous, with predominant rock types such as gravelly mixed soil, basalt, limestone, and sandstone(Yang et  
108 al., 2021) (Fig.1b). The region is extensively covered by weak rock formations and loose materials, and the area has  
109 undergone multiple tectonic movements, leading to fractured and jointed bedrock. Active fault zones, such as the  
110 Zemuhe and Xiaojiang fault zones, are also present in the region(Dun et al., 2023) (Fig.1c), with a predominantly



111 north-south orientation and left-lateral strike-slip motion. After the reservoir impoundment, fluctuations in water levels,  
112 prolonged immersion of the slopes by reservoir water, and seasonal dry-wet cycles contribute to the formation of a  
113 high-risk environment for geological hazards, including landslides, collapses, and debris flows.



114  
115 **Figure 1: Overview of the Study Area**

## 116 2.2 Research Data

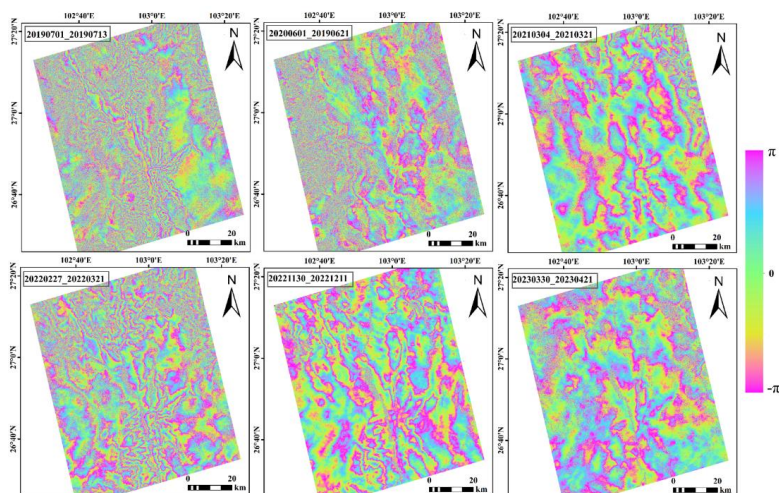
### 117 2.2.1 HyP3 InSAR Data

118 This study uses the HyP3 interferometric data stack, produced by the Alaska Satellite Facility (ASF) cloud platform,  
119 as the experimental dataset for interferometric baseline optimization and atmospheric error correction. The data can be  
120 accessed and freely applied for online retrieval through the ASF website (<https://search.asf.alaska.edu/#/>), with the  
121 application submitted on May 18, 2023. HyP3 is primarily used for processing Sentinel-1 data provided freely by the  
122 European Space Agency (ESA). Based on the ASF data platform, users can retrieve and query the Sentinel-1 SAR data  
123 archive. The main interferometric products available include wrapped and unwrapped interferograms, coherence maps,  
124 amplitude images, water mask images, DEMs, and look vector maps, etc. HyP3 utilizes Amazon's infrastructure  
125 services, including Amazon Elastic Compute Cloud (EC2) and Amazon Simple Storage Service (S3). It provides users  
126 with customized, on-demand synthetic aperture radar (SAR) processing services, eliminating the need for users to  
127 purchase or install complex SAR processing software and acquire advanced SAR processing skills. After the user  
128 submits an application through the ASF Vertex website or using the HyP3 Python SDK, the system automatically  
129 processes the interferometric data using GAMMA software hosted by Amazon Web Services (AWS). The process uses



130 the Copernicus GLO-30 DEM to remove terrain phases and applies the minimum cost flow (MCF) method for phase  
131 unwrapping, ultimately generating interferometric products suitable for coherence analysis and with moderate pixel  
132 spacing. HyP3 data effectively addresses the issues associated with traditional interferometric processing methods,  
133 which require significant disk space, computational resources, and processing time, offering a new approach for large-  
134 scale reservoir bank landslide detection and monitoring.

135 The HyP3 platform supports customizable temporal and spatial baseline settings. Considering the monthly variation in  
136 vegetation coverage in deep-cut mountain canyon areas, and to avoid phase unwrapping issues and the introduction of  
137 additional errors, this study sets the temporal baseline threshold to 36 days. Notably, the Sentinel-1 satellite has a  
138 relatively short revisit cycle, and it revisits the same location multiple times over short spatial distances, making the  
139 impact on coherence negligible. Therefore, no spatial baseline threshold is set. Long-term interferograms from July  
140 2019 to May 2023 were obtained using the baseline tool provided by the HyP3 online service platform (Fig.2)



141  
142 **Figure 2: Partial HyP3 Interferogram Stack Covering the Study Area.**

### 143 2.2.2 Auxiliary Datasets

144 The auxiliary datasets used in this study include several key sources. Sentinel-2 data (Level 2A) with a 10-meter spatial  
145 resolution, including red, blue, and green bands, was utilized to refine the estimation of surface vegetation coverage  
146 (Fraction of Vegetation Coverage, FVC) in the study area. This data was accessed online from Copernicus on June 18,  
147 2023. Additionally a 30-meter resolution Digital Elevation Model (DEM) from the ALOS WORLD 3D dataset,  
148 provided by the Japan Aerospace Exploration Agency (JAXA), was used to calculate topographic features like



149 mountain shadow, slope, aspect, and curvature. This dataset was accessed on July 1, 2023, from ALOS.High-resolution  
 150 Google Earth imagery with a 0.2-meter spatial resolution was employed for location annotation of reservoir-bank  
 151 landslides and for overlaying the acquired InSAR deformation results. This data was accessed on July 10, 2023, from  
 152 Google Earth. Drone aerial imagery with a 0.1-meter resolution was also used for field surveys to validate landslide  
 153 identification results and to observe the Optical Characteristics of typical reservoir-bank landslides, with the imaging  
 154 conducted on May 14, 2023.Precipitation data, acquired from the precipitation processing system on July 15, 2023,  
 155 were used to analyze rainfall patterns, and Reservoir water-level elevation data were measured in the field during the  
 156 research period. These datasets, summarized in Table. 1, provided comprehensive support for the research.

157 **Table 1: Data sources and specifications**

Data Name	Data Phase	Data Type	Data Scale	Data Source
Hyp3 Interferogram Stacking	2019-07~2023-05	Raster	40 m	ASF
Sentinel-2	2019-07~2023-05	Raster	10 m	ESA
FVC	2019-07~2023-05	Raster	30 m	Band Calculation
Elevation	-	Raster	30 m	JAXA
Google Maps imagery	2023	Raster	0.2 m	Google Earth
Drone Aerial Imagery	2023	Raster	0.02 m	Measured
Precipitation	2019-07~2023-05	-	-	PPS
Reservoir water-level elevation	2021-04~2023-05	-	-	Measured

158 **3 Research Methods and Data Processing**

159 The main technical process of this study is as follows: (1) calculation of vegetation coverage and classification of  
 160 interferogram stacks; (2) interferometric baseline optimization and atmospheric error correction; (3) surface  
 161 deformation information acquisition and reservoir bank landslide identification and monitoring.

162 **3.1 Vegetation Coverage Calculation Based on the Pixel Dichotomy Method**

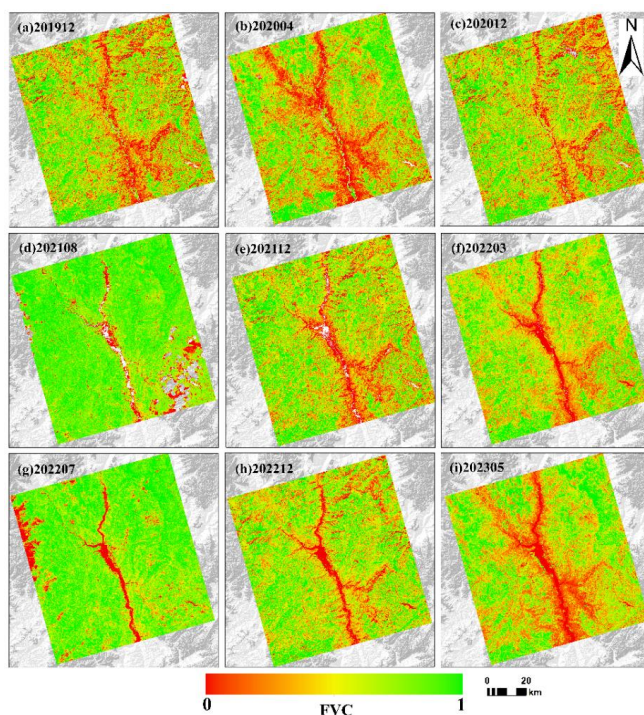
163 This study utilizes Sentinel-2 optical imagery from July 2019 to May 2023 and employs the Band Math tool to calculate  
 164 the Normalized Difference Vegetation Index (NDVI) across the study area. To minimize the influence of non-  
 165 landslide-related surface features, NDVI values were processed based on the pixel dichotomy model (Pi et al., 2021)  
 166 to derive the Fractional Vegetation Cover (FVC) on a monthly scale (Fig. 3), as expressed in Eq.(3)presents the spatial



167 and temporal variations in FVC, clearly reflecting seasonal vegetation dynamics—higher vegetation coverage is  
 168 observed in summer months (e.g., August 2020 and July 2022), while markedly lower values appear during winter  
 169 periods (e.g., December 2019 and December 2022). These seasonal changes in vegetation coverage significantly  
 170 impact interferometric coherence and phase unwrapping performance in SBAS-InSAR processing. The vegetation  
 171 temporal patterns revealed in FVC maps serve as a critical foundation for the development of the proposed Vegetation-  
 172 Adaptive WCTM, enabling dynamic adjustment of coherence thresholds to mitigate decorrelation effects associated  
 173 with vegetation growth cycles in deeply incised mountainous canyon environments.

$$174 \quad FVC = \begin{cases} 0 & , NDVI \leq NDVI_{soil} \\ \frac{NDVI - NDVI_{soil}}{NDVI_{veg} - NDVI_{soil}} & , NDVI_{soil} \leq NDVI \leq NDVI_{veg} \\ 1 & , NDVI \geq NDVI_{veg} \end{cases} \quad (1)$$

175 In the Eq.: *FVC* represents the monthly average vegetation coverage, *NDVI* represents the total value of the vegetation  
 176 index for the pixel, *NDVI<sub>soil</sub>* represents the *NDVI* value of pixels with no vegetation coverage, and *NDVI<sub>veg</sub>*  
 177 represents the *NDVI* value of pixels fully covered by vegetation.



178  
 179 **Figure 3: Temporal Vegetation Coverage in Partial Areas of the Study Region.**



180 **3.2 WCTM Optimization of Interferometric Baseline**

181 The WCTM considers the monthly variation of vegetation coverage in the time series and divides the interferogram  
182 into different coherence segments based on the vegetation coverage levels. The number of interferograms in each  
183 coherence segment is calculated, and the coherence coefficient is assigned a weight according to the number of  
184 interferograms in each segment. The final coherence coefficient optimization threshold is determined using a weighted  
185 averaging model. The process of optimizing the interferometric baseline using WCTM is as follows:

186 (1) Calculate the point coherence and average coherence for each interferogram. Coherence is an important indicator  
187 for describing the quality of the interferometric phase. It is defined by the cross-correlation function during the  
188 registration of two complex images. The coherence at a pixel point  $(i, j)$  in the interferogram is defined as:

$$189 \quad r_{(i,j)} = \frac{\left| \sum_{i=1}^m \sum_{j=1}^n M(i, j) S^*(i, j) \right|}{\sqrt{\sum_{i=1}^m \sum_{j=1}^n |M(i, j)|^2 \sum_{i=1}^m \sum_{j=1}^n |S(i, j)|^2}} \quad (2)$$

190 In the formula:  $(i, j)$  represents the pixel coordinates of the interferogram at a certain point in the radar slant range  
191 coordinates,  $m$  and  $n$  represent the local window sizes for coherence calculation, and  $M$  and  $S$  represent the  
192 acquisition of two different Synthetic Aperture Radar (SAR) data.  $*$  represents the complex conjugate of a given  
193 complex number.

194 After calculating the pixel coherence point by point, the coherence for each interferogram in the study area can be  
195 calculated using Eq. (3):

$$196 \quad r_{avg} = \frac{\sum_{i=1}^P \sum_{j=1}^Q r_{(i,j)}}{P * Q} \quad (3)$$

197 In the formula,  $r_{avg}$  represents the coherence coefficient of each interferogram, with a value range from 0 to 1.  $(i, j)$   
198 denotes the pixel coordinates of the interferogram at a specific point in radar slant-range coordinates.  $r_{(i,j)}$  represents  
199 the coherence at the pixel point  $(i, j)$ , and  $P$  and  $Q$  represent the length and width of the interferogram image,  
200 respectively.

201 (2) Classify the vegetation coverage levels of the time series.

202 (3) Divide the interferograms into different coherence segments.

203 (4) Assign weights to the coherence coefficients and use the weighted average model to optimize the coherence  
204 coefficient threshold. Calculate the number of interferograms under different vegetation coverage levels, assign  
205 weights to each coherence segment, and calculate the optimized interferometric baseline threshold based on the weights  
206 of different coherence segments:

$$207 \quad r_{WCTM} = \sum_{i=1}^I \frac{m_i r_i}{n} \quad (3)$$

208 In the Eq.:  $r_{WCTM}$  represents the optimized interferometric baseline threshold using the WCTM method,  $I$  represents  
209 the total number of coherence segments,  $m_i$  represents the number of interferograms in each coherence segment,  $r_i$



210 represents the average coherence of the interferograms in each coherence segment,  $n$  represents the total number of  
211 interferograms generated from all SAR acquisitions during the study period.

### 212 3.3 Correction of Atmospheric Delay Errors Using ECMWF ERA-5 Products

213 SAR signals are influenced by changes in atmospheric pressure, temperature, and humidity during propagation, leading  
214 to tropospheric delay effects(Li et al., 2023; Yang et al., 2023). The fifth-generation meteorological reanalysis dataset  
215 provided by European Centre for Medium-Range Weather Forecasts (ECMWF) offers high temporal resolution (hourly)  
216 and high spatial resolution (0.1 °), providing numerical weather model data on temperature, humidity, and pressure  
217 across 37 atmospheric pressure levels. This information can be effectively used to calculate atmospheric hydrostatic  
218 delay and correct atmospheric delay errors(Mandal et al., 2021; Soares et al.,2020).

$$219 \quad N = \left( k_1 \frac{P}{T} \right)_{hydro} + \left( k_2 \frac{e}{T} + k_3 \frac{e}{T^2} \right)_{wet} = N_{hydro} + N_{wet} \quad (5)$$

220 In the Eq.,  $N_{hydro}$  represents the fluid static refractive component of the atmospheric refractive index,  $N_{wet}$  represents  
221 the wet refractive component of the atmospheric refractive index,  $P$  is the total atmospheric pressure,  $T$  is the  
222 temperature in Kelvin,  $e$  is the water vapor pressure, and  $k$  is the empirical constant. At this point, the integral value  
223 of the refractive index between the tropospheric zenith direction  $h_{top}$  and the height along the radar line of sight  $h$   
224 is:

$$225 \quad \varphi_{tropo} = -\frac{4\pi}{\lambda} \cdot \frac{10^{-6}}{\cos\theta} \int_h^{h_{top}} (N_{hydro} + N_{wet}) dh \quad (6)$$

226 In the Eq.,  $\varphi_{tropo}$  represents the bidirectional tropospheric delay phase,  $\lambda$  denotes the radar center wavelength, and  
227  $\theta$  is the satellite incidence angle.

228 For InSAR measurements, the tropospheric delay phase in the interferogram is the difference in tropospheric delay  
229 between the imaging points of the master and secondary images. Due to slight differences in atmospheric conditions  
230 between the two acquisitions, the tropospheric delay error for two imaging points  $(q, p)$  at times  $m$  and  $n$  can be  
231 expressed as:

$$232 \quad \Delta\varphi_{tropo} [(p, q), (t_m, t_n)] = [\varphi_{tropo}(p, t_n) - \varphi_{tropo}(p, t_m)] - [\varphi_{tropo}(q, t_n) - \varphi_{tropo}(q, t_m)] \quad (7)$$

### 233 3.4 SBAS-InSAR Processing

234 SBAS-InSAR technology efficiently synthesizes all available small baseline interferograms, selects coherent target  
235 points for modeling and calculation, and removes atmospheric delays via temporal filtering to obtain high spatial  
236 density surface deformation results(Fan et al., 2016; Zhang et al., 2012). In this study, we use the open-source software  
237 package Mintpy (The Miami InSAR Timeseries Software in Python) for SBAS-InSAR processing(Zhang et al., 2019).  
238 We load the selected ascending track interferogram stack from July 2019 to May 2023 into the Mintpy software. A



239 reference pixel with high coherence (we set the threshold) is chosen from a region far from the deformation area. Then,  
 240 the initial phase value  $\theta_n$  and estimated phase value  $\varphi_n$  are used to evaluate the quality of each pixel in the raw  
 241 phase time series, as shown in Eq. (8):

$$242 \quad r = \frac{1}{N^2 - N} \sum_{n=1}^N \sum_{k \neq n}^N e^{i\theta_{nk}} e^{-i(\varphi_n - \varphi_k)} \quad (8)$$

243 In the Eq.,  $N$  represents the number of SAR images,  $i$  refers to a single SAR image, and  $n$  and  $k$  represent the  
 244 wrapped phase interferograms collected at corresponding times. To ensure data quality and the accuracy of InSAR  
 245 measurements, the root mean square error (RMSE) of the residual phase is used to estimate the noise present in the  
 246 time series:

$$247 \quad RMSE_i = \sqrt{\frac{1}{N_\Omega} \sum_{p \in \Omega} \left( -\hat{\varphi}_{resid}^i(p) \cdot \frac{\lambda}{4\pi} \right)^2} \quad (9)$$

248 In the Eq.,  $i = [1, \dots, N]$  and  $\Omega$  represent reliable pixels selected from the temporal coherence mask,  $\lambda$  is the  
 249 radar center wavelength, and  $\hat{\varphi}_{resid}^i$  represents the redundant phase at time  $i$ . After applying the noise mask, the  
 250 average deformation rate in the study area is estimated from the time series using Eq. (10):

$$251 \quad v_{los} \cdot t_i + c = -\hat{\varphi}_{disp}^i \cdot \frac{\lambda}{4\pi} \quad (3)$$

252 In the Eq.,  $v_{los}$  represents the average deformation rate in the radar line-of-sight direction,  $t_i$  denotes the time of SAR  
 253 acquisition at time  $i$ ,  $c$  is the unknown deformation offset constant, and  $\hat{\varphi}_{disp}^i$  represents the displacement time series.

## 254 4. Results and Analysis

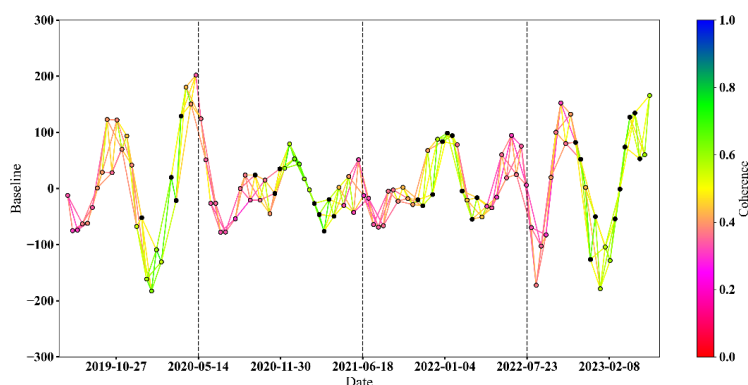
### 255 4.1 Results of Interference Baseline Optimization Using WCTM

256 Based on the 345 Hyp3 interferograms from July 2019 to May 2023, with July 3, 2019, as the reference image date,  
 257 the baseline connection map for all interferograms was obtained (Fig.4). It can be observed that the average coherence  
 258 coefficient in the Baihetan Reservoir area exhibits distinct seasonal variation, specifically with higher average  
 259 coherence during the winter and lower average coherence during the summer. This pattern aligns with seasonal changes  
 260 in vegetation and the regional dry-wet climate cycle.

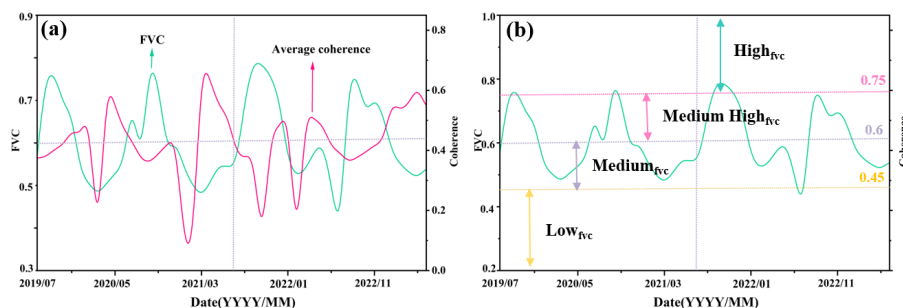
261 To further explore the relationship between the average coherence coefficient and vegetation coverage in the Baihetan  
 262 Reservoir area, monthly average vegetation coverage was calculated based on the pixel binary model (Eq (1)), and a  
 263 time series curve was established between the monthly average coherence of the interferograms and the vegetation  
 264 coverage (Fig.5a). The variation in the average coherence coefficient in the study area shows a significant correlation  
 265 with changes in vegetation coverage. The WCTM method proposed in this study was used to optimize the



266 interferometric baseline threshold. The monthly average vegetation coverage in the study area was classified into four  
 267 levels: low vegetation coverage (<45%), medium vegetation coverage (45%-60%), medium-high vegetation coverage  
 268 (60%-75%), and high vegetation coverage (>75%). Based on the classified vegetation coverage levels, the monthly  
 269 average coherence coefficient was divided into four coherence segments (Fig.5b). These segments accounted for 2.1%,  
 270 57.5%, 23.4%, and 17.0% of the total interferograms, respectively. These proportions were used as weights to calculate  
 271 the optimized interferometric baseline threshold ( $\lambda_{WCTM} = 0.4882$ ) using the WCTM method. Interferograms with  
 272 average coherence coefficients below this threshold were excluded, and the remaining 146 optimized interferograms  
 273 were retained for SBAS-InSAR processing.



274  
 275 **Figure 4: Spatio-Temporal Baseline Network of All Interferograms (The red dashed line represents a spatial baseline value**  
 276 **of 0, the black dashed lines indicate December 31 of each year, and the red-to-blue gradient represents the average coherence**  
 277 **of each interferogram).**



278  
 279 **Figure 5: Monthly Average Vegetation Coverage Time Series (a shows the relationship between monthly average vegetation**  
 280 **coverage and monthly average coherence coefficient; b presents the classification results of monthly average vegetation**  
 281 **coverage levels. The black dashed line represents the midpoint date of the study period).**



282 Due to the inherent limitations of C-band radar wavelength, coherence significantly deteriorates in areas with  
283 vegetation coverage exceeding 75% (particularly during summer, as shown in Figure 5a). This results in the omission  
284 of small-scale landslides within steep canyon slopes ( $>45^\circ$  inclination). Analysis using 30m-resolution ALOS DEM  
285 data indicates such terrain accounts for approximately 12.7% of the total study area. Future investigations could  
286 enhance detection capabilities through integration with L-band SAR data.

#### 287 **4.2 Early Detection Results of Reservoir-bank landslides**

288 The SBAS-InSAR processing was performed on the Hyp3 interferometric stack optimized using the WCTM method  
289 with the open-source software MintPy 1.5.1. Additionally atmospheric delay errors in the interferometric stack were  
290 corrected using the ECMWF ERA-5 product. As a result, radar line-of-sight surface deformation information from  
291 July 2019 to May 2023 was successfully obtained. Positive deformation values indicate motion towards the sensor,  
292 while negative values indicate motion away from the sensor. The absolute value of the deformation rate represents the  
293 magnitude of the deformation rate.

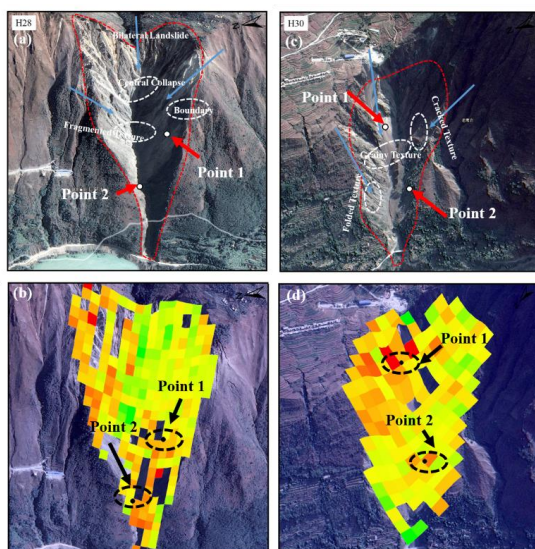
294 Based on relevant literature and the complex geological conditions in the Baihetan Reservoir area, C-band SAR data  
295 can be used to monitor slope deformation. In this region, if the annual deformation rate of a slope exceeds 16 mm, it  
296 is considered to indicate potential landslide hazards. In this study, considering factors such as resettlement activities,  
297 frequent human activities, and deformation signal errors within the reservoir area, a threshold of 16 mm/yr was set for  
298 identifying potential reservoir-bank landslides. Specifically, when the deformation rate of a slope exceeds 16 mm/yr,  
299 it is considered a suspected landslide area. To further assess landslide risks, this study combined SAR deformation  
300 signals with the established threshold to initially delineate suspected landslide areas. Additionally high-resolution  
301 optical images (e.g., Google Earth imagery) were used to conduct a detailed analysis of features such as color, structure,  
302 topographic morphology, landslide boundaries, and cracks for early detection and localization of reservoir-bank  
303 landslides(Fig.6).

304 A total of 39 potential reservoir-bank landslides were identified in the Baihetan Reservoir area Among the early  
305 identified landslides, 27 were historical landslide hazards, numbered H1-H27; 12 new landslides were identified,  
306 numbered H28-H39. The interpretation of the remote sensing images is shown in( Fig.7).





315 using Google Earth imagery. The high-resolution Google Earth imagery clearly shows prominent landslide features  
316 such as cracks, front bulging, subsidence, and slope surface fragmentation. The H28 landslide is located in Miansha  
317 Village, Qiaojia County, on the eastern bank of the upper reservoir area of the Jinsha River. InSAR deformation signals  
318 (Fig.8b) show two significant deformation zones at the right slip surface and the bottom of the slope. The Google Earth  
319 imagery reveals that both sides of the mountain slide toward the center, forming a large "bidirectional landslide" with  
320 an irregular shape, wider at the upper edge and narrower at the lower edge. Due to the steep slope, the slope surface  
321 shows significant subsidence features with rough textures (Fig.8a). Granular debris can be seen in the bottom trough,  
322 and the right slope surface shows more pronounced displacement traces compared to the left slope, suggesting that  
323 this landslide is highly likely to be in a long-term sliding state. The H30 landslide is located on the western bank of the  
324 lower reservoir area of the Baihetan Reservoir, in Shuicangzi Village, Huiedong County. The slope has a "tongue-  
325 shaped" irregular landslide perimeter with significant concave features. From the imagery, it is clear that the  
326 deformation of the slope is mainly caused by compressive deformation from the edges toward the center (Fig. 8c), and  
327 the deformation on the right slip surface is stronger than that on the left slip surface. In the middle of the landslide,  
328 small cracks and debris accumulation are visible, with strong deformation zones observed on the left side of the upper  
329 edge and the right side of the bottom (Fig.8d).

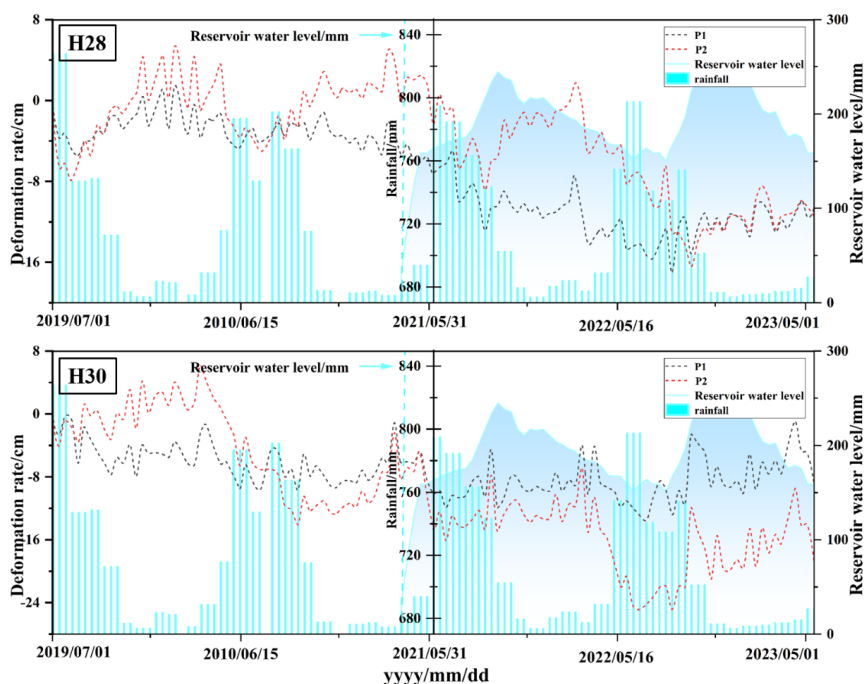


330  
331 **Figure 8: Remote sensing interpretation of optical characteristics and InSAR deformation signals of typical reservoir-bank**  
332 **landslides based on Google Earth imagery. Image source: © Google, Landsat / Copernicus, U.S. Navy, NGA, GEBCO.**



333 This study analyzes the temporal evolution of reservoir bank landslide deformation, selecting strong deformation  
334 characteristic points from the H28 and H30 landslide areas of the Baihetan Reservoir to establish time-series  
335 deformation curves (Fig.9). The landslide points, Point 1 and Point 2, are located at different elevations of the H28  
336 landslide and show a deformation trend moving away from the satellite in the radar line-of-sight direction. Precipitation  
337 and reservoir water storage in the Baihetan Reservoir are the main controlling factors of landslide deformation. When  
338 the reservoir water level reached its maximum elevation of 816.5m during the 2021 impoundment period (Fig.9 H28),  
339 the cumulative deformation at both characteristic points exceeded 10 cm before and after the water storage, indicating  
340 a strong response of the H28 landslide to changes in the reservoir water level. After the phased water storage period  
341 ended, Point 1 and Point 2 at different elevations showed different deformation fluctuations. Point 2, at a lower  
342 elevation, exhibited a stable deformation trend, possibly due to increased slope density and reduced looseness as a  
343 result of the rising water level. Additionally the deformation trends of Point 1 and Point 2 did not synchronize with the  
344 water level changes during the two water storage cycles, suggesting a time-lag effect of the landslide deformation in  
345 response to water level variations.

346 For the H30 landslide, Point 1 and Point 2 were selected, located at different elevations on the left and right slip surfaces.  
347 Both showed a deformation trend moving away from the satellite before and after water storage. Both points exhibited  
348 a deformation trend moving away from the satellite before and after water storage (Fig.9 H30). Compared to Point 2,  
349 Point 1's deformation trend was more stable, indicating that the H30 landslide may have rotational characteristics, with  
350 the sliding direction changing with the elevation of the slip surface. Particularly during the two water storage periods  
351 in 2021 and 2022, the deformation peaks of Point 1 and Point 2 did not coincide with the water level peaks (816.5m  
352 on September 30, 2021, and 825m on October 24, 2022), indicating a lag in the landslide's response to water level  
353 changes. Furthermore, after water storage, the deformation of Point 6 exceeded 10 cm, suggesting that water level  
354 changes may have further exacerbated the landslide in this region. In conclusion, the landslide changes are significantly  
355 affected by the water level, and real-time monitoring and updating of the reservoir bank landslide status are crucial for  
356 regional geological disaster prevention and mitigation efforts.



357  
358 **Figure 9: Time Series Deformation Curves of Typical Landslide Feature Points**

359 **5 Discussion and Conclusion**

360 **5.1 Discussion**

361 **5.1.1 Baseline Optimization Performance Evaluation**

362 The WCTM method proposed in this paper takes into account the relationship between the InSAR coherence and the  
 363 monthly variation in vegetation cover, which represents a specific improvement over previous studies. By comparing  
 364 the WCTM method with traditional interference baseline selection methods (short time-space baseline threshold and  
 365 average coherence threshold), the performance of the optimized interferometric baseline is evaluated through the  
 366 calculation of deformation rate standard deviation (Fig.10 and Fig.11) and the full-phase ambiguity of the loop closure  
 367 error (Fig.12). As shown in Fig 10, the deformation rate standard deviation with the short time-space baseline threshold  
 368 (time baseline threshold: 36d, space baseline threshold: 200m) exhibits an irregular and uneven spatial distribution  
 369 along the Jinsha River (from south to north), with maximum and minimum deformation rate standard deviations  
 370 observed in the northern and southern parts of the study area, respectively (Fig.10a). This indicates that the short time-  
 371 space baseline threshold is prone to introducing decorrelation errors, making it ineffective for obtaining stable InSAR



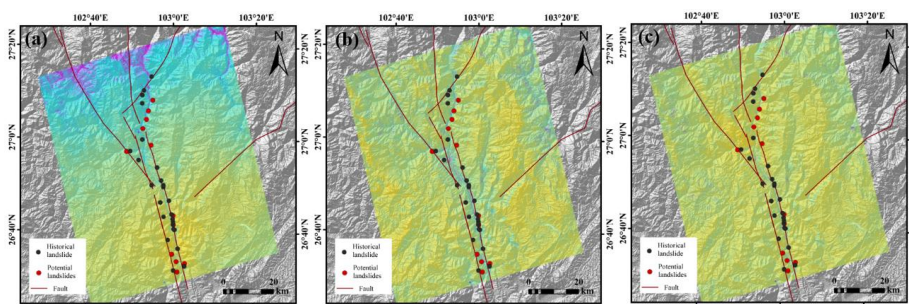
372 deformation signals. The use of the average coherence threshold effectively improves the overall Stability of the InSAR  
373 signals, but some anomalies were still observed outside the reservoir banks of the Baihetan Reservoir (Fig.10b). This  
374 suggests that simply setting an average coherence threshold through basic statistical methods does not reflect the  
375 seasonal variation in coherence caused by interference, and is not suitable for InSAR deformation signal detection in  
376 deeply-cut mountain canyon areas. The WCTM method, which optimizes the interferometric baseline by considering  
377 the relationship between coherence and vegetation cover, reduces the redundancy of low-coherence interferograms,  
378 effectively improving overall coherence, and avoids the subjectivity caused by expert experience and simple statistical  
379 methods. The deformation rate standard deviation shows a more uniform and Stable distribution (Fig.10c). Furthermore,  
380 the statistical analysis of the deformation rate standard deviation distribution (Fig.12) also confirms this, with the  
381 average deformation rate standard deviations for the short time-space baseline method, average coherence threshold  
382 method, and WCTM method being 1.7865, 1.4587, and 1.2668, respectively, and with quartile medians of 1.6802,  
383 1.3831, and 1.1667. This demonstrates that the WCTM method, which optimizes interferometric baseline thresholds  
384 significantly reduced the time-series noise contained in the InSAR deformation signals, resulting in more effective and  
385 stable deformation rates.

386 The WCTM method optimizes interferometric baseline thresholds, substantially reducing temporal noise in InSAR  
387 deformation signals, thereby yielding more reliable and stable deformation rate estimates. The relative reduction in the  
388 deformation rate standard deviation achieved by the WCTM method compared to the conventional short temporal  
389 baseline threshold method is quantitatively expressed as:

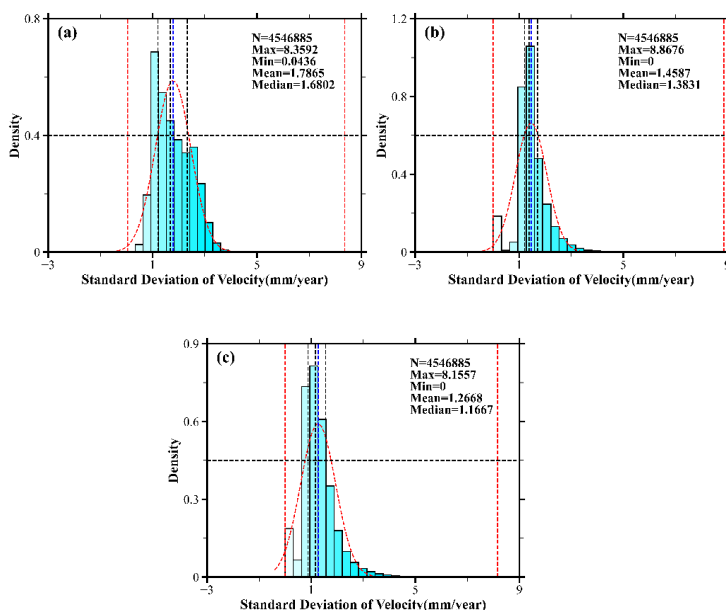
$$390 \quad Reduction = \frac{\sigma_{shortbaseline} - \sigma_{WCTM}}{\sigma_{shortbaseline}} \times 100\%$$

391 (2)

392 Where  $\sigma_{shortbaseline}$  and  $\sigma_{WCTM}$  denote the mean deformation rate standard deviations obtained by the short  
393 temporal baseline threshold method and the proposed WCTM method, respectively. This result quantitatively  
394 demonstrates that the WCTM method reduces the deformation rate standard deviation by approximately 29.1%,  
395 confirming its superior capability in improving the accuracy and stability of deformation measurements in complex  
396 mountainous canyon environments.



397  
 398 **Figure 10: Standard Deviation of Deformation Rates: (a) Results without interferometric baseline threshold optimization,**  
 399 **(b) Results with interferometric baseline optimization based on average coherence, (c) Results with interferometric baseline**  
 400 **optimization using the WCTM method**

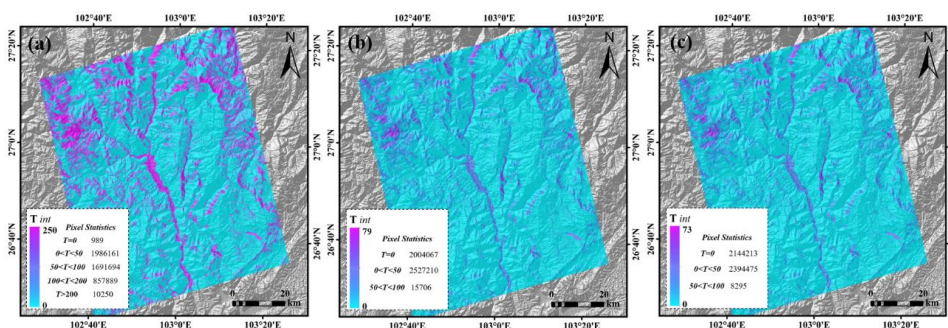


401  
 402  
 403  
 404 **Figure11: Statistical Distribution of Deformation Rate Standard Deviation**

405 In addition, the full-phase ambiguity results of the loop phase closure check for phase unwrapping also validate the  
 406 performance of the optimized interferometric baseline using the WCTM method proposed in this paper. The full-phase  
 407 ambiguity of the loop closure describes the "periodicity" or "ambiguity" of radar phase during the phase unwrapping  
 408 process in time-series InSAR technology, and is used to evaluate the quality of phase unwrapping and possible phase  
 409 unwrapping errors. Fig.12 shows the full-phase ambiguity of the loop closure obtained using the three methods. It is  
 410 not difficult to observe that, compared to the short time-space baseline threshold method, the optimization of  
 411 interferometric baseline threshold using the coherence coefficient of the interferogram yields more robust phase



412 unwrapping results, with a significant improvement in the quality of phase unwrapping. The non-zero values of the  
413 full-phase ambiguity of the loop closure are effectively reduced. By considering the monthly variation of InSAR  
414 coherence and vegetation cover, the WCTM method leads to an increase of 140,146 good unwrapping results ( $T_{int} =$   
415 0) compared to the average coherence threshold method, while the unwrapping errors with closure differences greater  
416 than 50 ( $50 \text{ times } 2\pi$ ) are reduced by 7,411, indicating that the WCTM method effectively reduces the noise level  
417 detected by time-series InSAR technology and demonstrates good applicability in deeply-cut mountain canyon areas.  
418



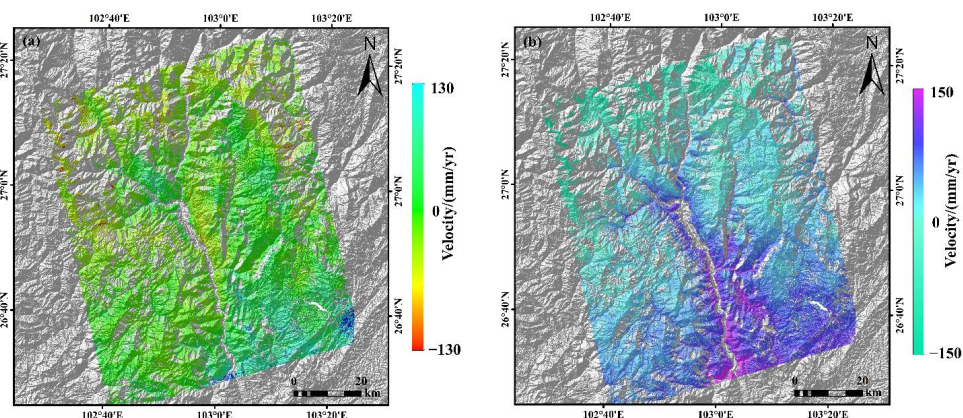
419  
420 **Figure 12: Integer Ambiguity of Circular Phase Closure Errors**

### 421 5.1.2 SBAS-InSAR Deformation Signal Accuracy Verification and Error Analysis

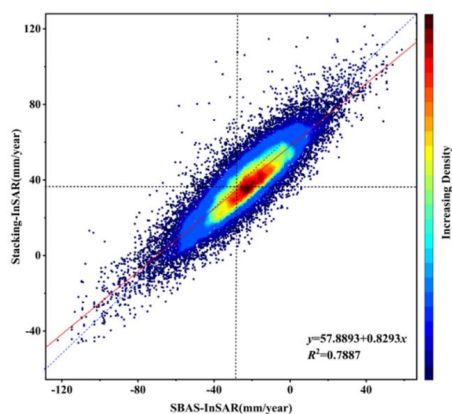
422 This paper describes a method for optimizing the interferometric baseline threshold of the Hyp3 interferogram stack  
423 using the proposed WCTM method to obtain InSAR deformation signals for deeply incised high mountain canyon  
424 areas. The accuracy of the deformation signals is limited by the Hyp3 interferogram stack products processed and  
425 released by the ASF. Due to the special terrain and topography of the Baihetan Reservoir area, the descending track  
426 data experiences significant geometric distortion. To improve the accuracy of the InSAR deformation signals and  
427 reduce the impact of geometric distortion on reservoir bank landslide identification results, we selected ascending track  
428 data from the Hyp3 interferogram stack as the experimental dataset for the WCTM method. By comparing with  
429 historical landslide data from 2021, the spatial locations of the early-identified reservoir-bank landslides showed a high  
430 degree of similarity to the historical landslides, indirectly validating the accuracy of the InSAR results. However, due  
431 to the lack of GNSS observational data in the study area, we were unable to compare the detected InSAR deformation  
432 signals with GNSS data on a time-series scale. To quantitatively analyze the reliability of the InSAR results, we  
433 performed cross-validation by comparing deformation results obtained using different techniques on the same track.  
434 We used the Hyp3 interferogram stack mentioned in Section 2.2 for Stacking-InSAR processing, obtaining the average



435 phase velocity for the study period( Fig.13b), and then performed a combined analysis with the deformation rates  
 436 obtained using the SBAS-InSAR technique in Section 4.3. We randomly selected 25,141 deformation points from areas  
 437 with consistent deformation trends (Fig.13) for regression analysis (Fig.14). The cross-validation results between  
 438 SBAS-InSAR and Stacking-InSAR show an  $R^2$  value of 0.79, which demonstrates that the surface deformation  
 439 information obtained from both SBAS-InSAR and Stacking-InSAR methods is reliable on both temporal and spatial  
 440 scales. Additionally, the cross-validation results also verify the accuracy and reliability of the time-series InSAR data  
 441 optimized using the WCTM method proposed in this study.



442  
 443 **Figure 13: Deformation Information from SBAS-InSAR and Stacking-InSAR in the Study Area**

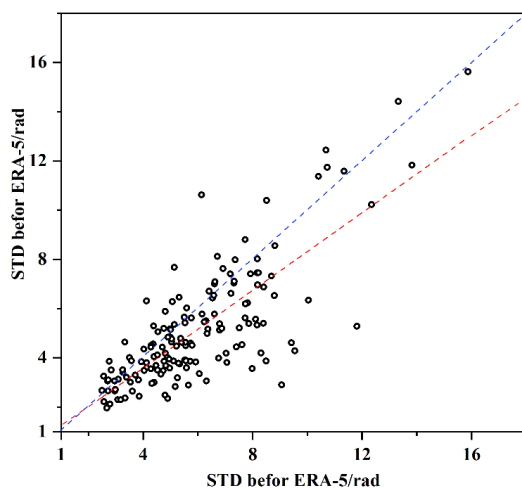


444  
 445 **Figure 14: Cross-validation Results between Stacking-InSAR and SBAS-InSAR**

446 The SBAS-InSAR deformation inversion results are often affected by phase unwrapping errors and atmospheric delay  
 447 errors. Optimizing these errors can significantly improve monitoring accuracy. The above experiments demonstrate  
 448 that by adjusting the coherence threshold and optimizing the full-wavelength ambiguity of the phase closure, the



449 WCTM method effectively improves the stability of phase unwrapping. Based on this, this study combined the ERA-  
450 5 meteorological reanalysis product released by the ECMWF to correct atmospheric delay errors, and compared the  
451 phase standard deviation of interferograms before and after correction (Fig.15). The results show that after ERA-5  
452 correction, the phase standard deviation significantly decreased, with the maximum phase standard deviation reduced  
453 from 11.81 rad to 5.27 rad. Notably, 71.2% of the interferogram phase standard deviations showed significant  
454 improvement, while only 28.8% of interferograms were negatively affected, with the maximum negative standard  
455 deviation being  $-4.48$  rad. This indicates that the ERA-5 product, with its high spatiotemporal resolution, can  
456 effectively eliminate atmospheric delay errors in InSAR monitoring, and is particularly well-suited for deep-cut  
457 mountain canyon areas.



458

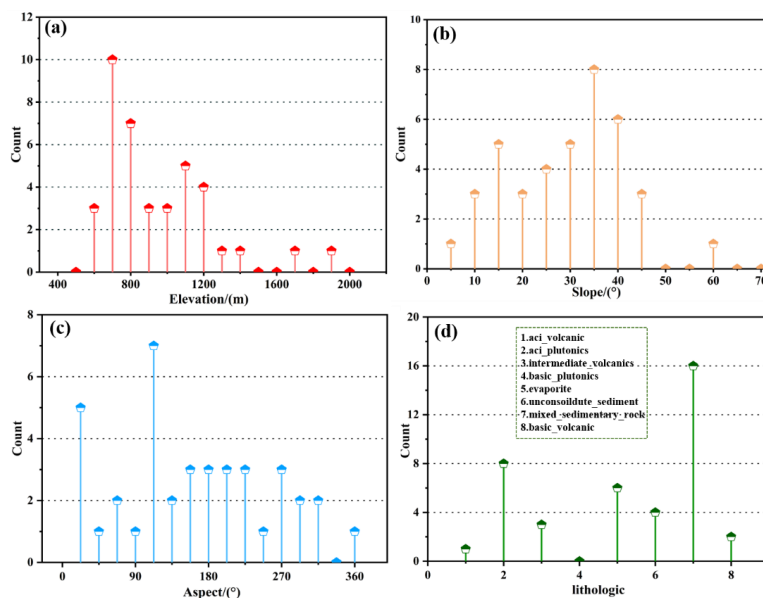
459 **Figure 15: Correlation Analysis of Phase Standard Deviation Before and After ERA-5 Atmospheric Correction**

### 460 **5.1.3 Distribution Patterns of Reservoir-bank landslides and the Impact of Reservoir Water Level Changes on** 461 **Landslide Deformation**

462 There are many factors that influence reservoir-bank landslides. Considering the geomorphological conditions of the  
463 Baihetan Reservoir, this study analyzes the distribution patterns of reservoir-bank landslides based on the 39 landslides  
464 identified in Section 4.2, using statistical methods and examining terrain factors such as elevation, slope, aspect, and  
465 lithology (Fig.16). From Fig16, it can be seen that the identified reservoir-bank landslides are primarily concentrated  
466 within the elevation range of 600m to 1400m and widely developed in slopes ranging from  $30^\circ$  to  $45^\circ$ . This indicates  
467 that slopes that are too gentle are not enough to induce slope movement, while steeper reservoir banks are more  
468 conducive to landslide development. The landslides identified in the early stages are mostly distributed in the northeast,



469 east, and northwest directions, similar to the findings of Dun et al., with fewer landslides identified in the north-south  
 470 direction. This could be due to the sensitivity of the Sentinel-1 satellite to deformation in the north-south direction  
 471 being affected by its flight path. Additionally, the lithology of the reservoir-bank landslides mainly consists of mixed  
 472 sedimentary rocks, carbonate rocks, and neutral volcanic rocks, which are generally located in incompetent strata.  
 473 Previous studies suggest that the increase or decrease in pore water pressure on the sliding surface caused by changes  
 474 in the reservoir water level is the primary factor triggering instability in reservoir-bank landslides. Moreover, under  
 475 different reservoir water level change patterns, the deformation signals of the landslides show significant differences.  
 476 Notably, in Section 4.3, the analysis of landslide deformation trend evolution indicates that the peak of landslide  
 477 deformation does not coincide with the peak of the reservoir water level, suggesting a time-lag response of landslide  
 478 deformation to the water level changes in the Baihetan Reservoir. This phenomenon is similar to previous research. The  
 479 time-lag effect includes a time delay in the deformation process of the landslide and irreversible plastic deformation  
 480 of the landslide's geological structure during the water level change process. As the pore water pressure in the landslide  
 481 changes, it affects the stability of the slope. The stress state of the soil also needs time to adjust to and adapt to the new  
 482 pressure conditions. Therefore, when the reservoir water level changes, the moisture within the landslide requires a  
 483 certain period to reach a new equilibrium state, which is why the deformation of the reservoir-bank landslides shows  
 484 a clear lag response to water level fluctuations.



485

486

Figure 16: Statistical Chart of the Distribution Pattern of Reservoir-bank landslides



487 **5.2 Conclusion**

488 This study focused on the Baihetan Hydropower Station reservoir area, utilizing Sentinel-1A ascending and descending  
489 track data from July 2019 to May 2023. The Vegetation-Adaptive WCTM was employed to optimize interferometric  
490 baseline thresholds, combined with atmospheric delay correction using the ERA-5 meteorological reanalysis product.  
491 The main conclusions are as follows:

492 (1) Compared with the traditional short temporal-spatial baseline threshold method and the average coherence  
493 threshold method, the WCTM approach achieved an average reduction of 0.520 and 0.192 in the standard deviation  
494 (STD) of deformation signals, and median reductions of 0.514 and 0.216, respectively, significantly improving phase  
495 unwrapping quality. After atmospheric delay correction, 71.2% of the interferograms exhibited a substantial decrease  
496 in phase STD, with the maximum phase STD was reduced from 11.81 rad to 5.27 rad. These results demonstrate the  
497 superiority of the proposed method in enhancing data quality.

498 (2) Using the InSAR deformation signals optimized by the WCTM, early identification of reservoir-bank landslides in  
499 deeply incised mountainous canyon areas was successfully achieved, with a total of 39 landslides detected. Field  
500 validation via drone surveys confirmed the applicability and robustness of the method, and detailed analyses of the  
501 spatial distribution and temporal evolution of landslides were conducted.

502 (3) Statistical analysis revealed that most reservoir-bank landslides in the Baihetan area occur within an elevation range  
503 of 600 m to 1400 m and on slopes between 30° and 45°. The predominant slope aspects are northeast, east, and  
504 northwest. Lithologically, these landslides mainly develop on carbonate rocks, intermediate volcanic rocks, mixed  
505 sedimentary rocks, and siliceous clastic sedimentary rocks.

506 In summary, the WCTM method provides an effective technical means for high-precision monitoring of reservoir-  
507 bank landslides in complex mountainous regions, offering significant theoretical and practical value for regional  
508 landslide disaster prevention and mitigation.

509

510 **Code and data availability**

511 The data of this study are available upon request from any author. Please refer to the author information in the article  
512 for contact details.

513

514 **Authorship contribution statement**



515 All authors have made significant contributions to various aspects of this research. The specific contributions are as  
516 follows: XI Wenfei was responsible for writing, reviewing, and editing the manuscript; HONG Wenyu handled data  
517 management; YANG Zhiqian was responsible for conceptualization of the study; HUANG Guangcai was responsible  
518 for software development; GUO Junqi managed the project; YANG Kunwu performed formal analysis; JIN Tingting  
519 managed resources; All authors participated in various stages of the research and have approved the final version of  
520 the manuscript.

521

#### 522 **Competing interests**

523 The authors declare that there is no competing interest related to the publication of this paper.

524

#### 525 **Acknowledgment**

526 We would like to express our sincere gratitude to Yang Zhengrong for providing valuable experimental data and results  
527 during their master's study, which significantly supported the successful completion of this research. We also appreciate  
528 the use of the Hybrid Pluggable Processing Pipeline (HyP3) developed by HogensoDn et al. (2020), which offered a  
529 cloud-native infrastructure for SAR data processing and greatly facilitated our work.

530

#### 531 **Financial support**

532 This research was supported by the Basic Research Plan Outstanding Youth Fund Project of Yunnan Province (Grant  
533 No. 202401AV070010), the National Natural Science Foundation of China (Grant No. 41861134008), the Muhammad  
534 Asif Khan Academician Workstation of Yunnan Province (Grant No. 202105AF150076), the Key R&D Program of  
535 Yunnan Province (Grant No. 202003AC100002), the Major Scientific and Technological Projects of Yunnan Province  
536 on ecological environment monitoring and intelligent management of natural resources (Grant No. 202202AD080010),  
537 the Guizhou Scientific and Technology Fund (Grant No. QKHJ-ZK (2023) YB 193), and the Yunnan Province  
538 Innovation Team Project on sustainable development of plateau lakeside cities (Grant No. 202305AS350003).

539

#### 540 **Review statement**

541 No potential conflict of interest was reported by the author(s).

542

#### 543 **References:**

544 Liu, Y., Qiu, H., Yang, D., Liu, Z., Ma, S., Pei, Y., Tang, B. Deformation responses of landslides to seasonal rainfall  
545 based on InSAR and wavelet analysis, *J. L.*, 1-12, 2022.  
546 Li, X, E., Zhou, L., Su, F, Z., Wu, W, Z. Application of InSAR technology in landslide hazard: Progress and prospects.  
547 *J. National Remote Sensing Bulletin.*, 25(02): 614-629, 2021



- 548 Zhu, Y. R., Qiu, H. J., Liu, Z. J.; Ye, B. F., Tang, B. Z., Li, Y. J., Kamp, U. Rainfall and water level fluctuations  
549 dominated the landslide deformation at Baihetan Reservoir, China, *J. Journal of Hydrology*, 642. [https://doi:10.1016/j.jhydrol.2024.131871](https://doi.org/10.1016/j.jhydrol.2024.131871), 2024.
- 551 Lu, H., Li, W., Xu, Q., Dong, X., Dai, C., Wang, D. Early detection of landslides in the upstream and downstream areas  
552 of the Baige Landslide, the Jinsha River based on optical remote sensing and InSAR technologies, *J. Geomatics and  
553 Information Science of Wuhan University*, 44(9), 1342-1354, [https://doi:10.13203/j.whugis20190086](https://doi.org/10.13203/j.whugis20190086), 2019.
- 554 Yanhui, G., Xiaojuan, M., Liang, Z. Deformation characteristics and mechanism of Dahua giant ancient landslide deposit  
555 in the upper Lancang River valley. *Geological Bulletin of China*. 2025, 1-13.
- 556 Zhengjun, M., Munan, W., Xu, M., Jiabin, Z., Jing, Z. Research on Monitoring and Warning of Terraced Loess Potential  
557 Landslide Based on Data Fusion, *J. Geomatics and Information Science of Wuhan University*, 1-18, [https://doi:10.13203/j.whugis20240129](https://doi.org/10.13203/j.whugis20240129), 2024.
- 559 Jian'ao, C., Dongping, M., Wenyi, Z., Xiao, L., Xinxin, Z. Integrated remote sensing-based hazard identification and  
560 disaster-causing mechanisms of landslides in Zayu County, *J. Remote Sensing for Natural Resources*, 36(01): 128-136, 2024.
- 561 Guo, X. D., Zha, X. J., Huang, J. H. Monitoring Earthquake-triggered Landslide Using Optical Image Offset-tracking  
562 Algorithm, *J. Remote Sensing Information*, 31(03): 56-60, 2016.
- 563 Li, Z. H., Zhu, W., Yu, C., Zhang, G. Q., Zhang, C. L., Liu, Z. J., Zhou, J. W. Interferometric synthetic aperture radar  
564 for deformation mapping: opportunities, challenges and the outlook, *J. Acta Geodaetica et Cartographica Sinica*, 51(07):  
565 1485-1519, 2022.
- 566 Li, L., Hong, Y. T. Application of improved SBAS technology in monitoring mining land subsidence, *Science of  
567 Surveying and Mapping*, 45(10): 92-101, [https://doi:10.16251/j.cnki.1009-2307.2020.10.014](https://doi.org/10.16251/j.cnki.1009-2307.2020.10.014), 2020.
- 568 Zhou, Zh. W., Cheng, X., Zhou, W., Xiao, H. B., Li, K. L. Deformation monitoring on reservoir bank landslide of a  
569 hydropower station based on InSAR time series, *J. Yangtze River*, 53(08): 112-116, [https://doi:10.16232/j.cnki.1001-4179.2022.08.018](https://doi.org/10.16232/j.cnki.1001-4179.2022.08.018), 2022.
- 571 Ferretti, A., Prati, C., Rocca, F. Permanent scatterers in SAR interferometry, *J. IEEE Trans. Geosci. Remote Sens.*,  
572 39(1): 8-20, 2002.
- 573 Pepe, A. J. Multi-temporal small baseline interferometric SAR algorithms: Error budget and theoretical performance.  
574 *Remote Sens.* 2021, 13(4), 557.
- 575 Liao, M. S., Dong, J., Li, M. H., Ao, M., Zhang, L., Shi, X. G. Radar remote sensing for potential landslides detection and  
576 deformation monitoring, *J. Natl. Remote Sens. Bull.*, 25(01): 332-341, 2021.
- 577 Zebker, H. A., Pepin, K. Maximum temporal baseline for InSAR time series. Paper presented at the 2021 IEEE  
578 International Geoscience and Remote Sensing Symposium IGARSS. 2021.
- 579 Zhang, Z., Li, J., Duan, P., Chang, J. Creep identification by the baseline optimized TS-InSAR technique considering  
580 the monthly variation in coherence, *J. Geocarto International*, 2159071, 2022.
- 581 Yang, G., Qiu, H., Wang, N., Yang, D., & Liu, Y. Tracking 35-year dynamics of retrogressive thaw slumps across  
582 permafrost regions of the Tibetan Plateau, *J. Remote Sensing of Environment*, 325: 114786, 2025.
- 583 Liu, H., Song, C., Li, Z., Liu, Z., Ta, L., Zhang, X. A New Method for The Identification of Earthquake-damaged  
584 Buildings Using Sentinel-1 Multi-temporal Coherence Optimized by Homogeneous SAR Pixels and Histogram  
585 Matching. *IEEE Journal of Selected Topics in Applied Earth Observations and Remote Sensing*, 2024.
- 586 Ren, T., Gong, W., Gao, L., Zhao, F., Cheng, Z. An interpretation approach of ascending-descending SAR data for  
587 landslide identification, *J. Remote Sens.*, 14(5): 1299, 2022.
- 588 Wang, K., Chen, J. A New Method for Reconstructing Decorrelated InSAR Phase Measurements Over Densely Vegetated  
589 Natural Terrain. Paper presented at the IGARSS 2023-2023 IEEE International Geoscience and Remote Sensing  
590 Symposium. 2023.



- 591 Zhang, B., Liu, G., Wang, X., Fu, Y., Liu, Q., Yu, B., Li, Z. Semi-automated mapping of complex-terrain mountain  
592 glaciers by integrating l-band sar amplitude and interferometric coherence, *J. Remote Sens.*, 14(9), 1993, 2022.
- 593 Shi, G. Typical Urban Subsidence Revealed from Advanced Multitemporal SAR Interferometry: The Chinese  
594 University of Hong Kong (Hong Kong). 2019.
- 595 Zhao, C., Lu, Z., Zhang, Q., de La Fuente, J. Large-area landslide detection and monitoring with ALOS/PALSAR  
596 imagery data over Northern California and Southern Oregon, USA, *J. Remote sensing of environment.*, 124, 348-  
597 359, 2012.
- 598 Zhou, P., Liu, W., Zhang, X., Wang, J. Evaluating Permafrost Degradation in the Tuotuo River Basin by MT-InSAR  
599 and LSTM Methods, *J. Sensors.*, 23(3), 1215, 2023.
- 600 Tao, Q., Wang, F., Guo, Z., Hu, L., Yang, C., Liu, T. Accuracy verification and evaluation of small baseline subset  
601 (SBAS) interferometric synthetic aperture radar (InSAR) for monitoring mining subsidence, *J. European Journal of*  
602 *Remote Sensing.*, 54(1), 642-663, 2021.
- 603 Wang, Y., Xu, H., Zeng, G., Liu, W., Li, S., Li, C. A Method for Selecting SAR Interferometric Pairs Based on  
604 Coherence Spectral Clustering, *J. IEEE Trans. Geosci. Remote Sens.*, 61: 1-15, 2023.
- 605 Zhang, X., Gan, S., Yuan, X., Zong, H., Wu, X., Shao, Y. Early Identification and Characteristics of Potential Landslides  
606 in Xiaojiang Basin, Yunnan Province, China Using Interferometric Synthetic Aperture Radar Technology, *J.*  
607 *Sustainability.*, 16(11), 4649, 2024.
- 608 Dai, H., Zhang, H., Dai, H., Wang, C., Tang, W., Zou, L., Tang, Y. Landslide identification and gradation method based  
609 on statistical analysis and spatial cluster analysis, *J. Remote Sens.*, 14(18), 4504, 2022.
- 610 Westerhoff, R., Steyn-Ross, M. Explanation of InSAR phase disturbances by seasonal characteristics of soil and  
611 vegetation, *J. Remote Sens.*, 12(18), 3029, 2020.
- 612 Zhang, X., Li, Z., Liu, Z. Reduction of atmospheric effects on InSAR observations through incorporation of GACOS  
613 and PCA into small baseline subset InSAR. *IEEE Trans. Geosci, J. Remote Sens.*, 61, 1-15, 2023.
- 614 Lemmetyinen, J., Ruiz, J. J., Cohen, J., Haapamaa, J., Kontu, A. Pulliainen. Attenuation of radar signal by a boreal  
615 forest canopy in winter, *J. IEEE Geoscience and Remote Sensing Letters.*, 19, 1-5, 2020.
- 616 Chen, Y., Sun, Q., Hu, J. Quantitatively estimating of InSAR decorrelation based on Landsat-derived NDVI, *J. Remote*  
617 *Sens.*, 13(13), 2440, 2021.
- 618 Santoro, M., Wegmuller, U., Askne, J. Signatures of ERS–Envisat interferometric SAR coherence and phase of short  
619 vegetation: An analysis in the case of maize fields. *IEEE Trans, J. Geosci. Remote Sens.*, 48(4), 1702-1713, 2009.
- 620 Qiu, H., Li, Y., Zhu, Y., Ye, B., Yang, D., Liu, Y., Wei, Y. Do post-failure landslides become stable? *CATENA.*, 249:  
621 108699, 2025.
- 622 Li, L., Xu, C., Yao, X., Shao, B., Ouyang, J., Zhang, Z., Huang, Y. Large-scale landslides around the reservoir area of  
623 Baihetan hydropower station in Southwest China: Analysis of the spatial distribution, *J. Natural Hazards Research.*, 2(3),  
624 218-229, 2022.
- 625 XI, W. F. Study on remote sensing image preprocessing method and landslide feature identification of UAV in northeast  
626 Yunnan mountain area, *J. Acta Geodaetica et Cartographica Sinica.*, 49(08): 1071, 2020.
- 627 Shi, G. L., Chen, Q., Liu, X. W., Yang, Y. H., Xu, Q., Zhao, J. J. Deformation velocity field along Aspect direction of  
628 an ancient Landslide at TaoPing village derived from Ascending and Descending Sentinel-1A data, *J. Journal of*  
629 *Engineering Geology.*, 30(04): 1350-136, 2022.
- 630 Zhu, S. N., Yin, Y. P., Wang, M., Zhu, M., Wang, C. H., Wang, W. P., Zhao, H. Instability mechanism and disaster mitigation  
631 measures of long-distant landslide at high location in Jinsha River junction zone: case study of Slandslide in Jinsha  
632 River Tibet, *J. Chinese Journal of Geotechnical Engineering.*, 43(04): 688-697, 2021
- 633 Xie, M. W., Mowen, X.; Wang, Z. F., Hu, M., Huang, J. H. The Characteristic Analysis of D-InSAR Data for Landslides



- 634 Monitoring in Alpine and Canyon Region, *J. Bulletin of Surveying and Mapping.*, (04): 18-21+40, 2012.
- 635 Qing, Y. Study on Mineralization of lead-zinc deposits in Northeastern Yunnan and Northwestern Guizhou Pro-  
636 vince, China. Wuhan, China University of Geosciences, 2021.
- 637 Dun, J. W., Feng, W. K., Yi, X. Y., Zhang, G. Q., Wu, M. T. Early InSAR identification of active Landslide before  
638 impoundment in BaiHeTan Reservoir area--A case study of HULUKOU town XiangBiling section, *J. Journal of*  
639 *Engineering Geology.*, 31(02): 479-492, <https://doi:10.13544/j.cnki.jeg.2022-0016>, 2023.
- 640 Pi, X. Y., Zeng, Y. N., He, C. Q. High-resolution urban vegetation coverage estimation based on multi-source remote  
641 sensing data fusion, *J. Remote Sens.*, 25(06): 1216-1226, 2021.
- 642 Li, S. H., Dong, J., Zhang, L., Liao, M., S. Time-series InSAR tropospheric atmospheric delay correction based on common  
643 scene stacking, *J. Natl. Remote Sens. Bull.*, 27(10): 2406-2417, 2023.
- 644 Yang, W. T., Liu, G. L., Niu, C., Tao, L., X. Small scale atmospheric delay correction of SBAS-InSAR based on GACOS in  
645 subsidence monitoring, *J. Science of Surveying and Mapping.*, 48(06): 73-81, 2023.
- 646 Mandal, K., Saha, S., Mandal, S. Applying deep learning and benchmark machine learning algorithms for landslide  
647 susceptibility modelling in Rorachu river basin of Sikkim Himalaya, India, *J. Geoscience Frontiers*, 2(5),  
648 <https://doi:10.1016/j.gsf.2021.101203>, 2021.
- 649 Soares, P. M. M., Lima, D. C. A., Nogueira, M. Global offshore wind energy resources using the new ERA-5  
650 reanalysis, *J. Environmental Research Letters.*, 15(10), <https://doi:10.1088/1748-9326/abb10d>, 2020.
- 651 Fan, R. Y., Liao, J., Gao, S., Zeng, Q. M. Comparison Research of High Coherent Target Selection Based on In SAR Time  
652 Series Analysis, *J. Journal of Geo-information Science.*, 18(06): 805-814, 2016.
- 653 Zhang, X. D., Ge, D. Q., Wu, L. X., Zhang, L., Wang, Y., Guo, X. F., Yu, X. H. Study on monitoring land subsidence in mining  
654 city based on coherent target small-baseline InSAR, *J. Journal of China Coal Society.*, 37(10): 1606-1611,  
655 <https://doi:10.13225/j.cnki.jccs.2012.10.001>, 2012.
- 656 Zhang, Y. J., Fattahi, H., Amelung, F. Small baseline InSAR time series analysis: Unwrapping error correction and  
657 noise reduction, *J. Computers & Geosciences.*, 133, <https://doi:10.1016/j.cageo.2019.104331>, 2019.
- 658